

CoCoNet: Coupled Contrastive Learning Network with Multi-level Feature Ensemble for Multi-modality Image Fusion

Jinyuan Liu^{1,3}, Runjia Lin^{1,3}, Guanyao Wu^{1,3}, Risheng Liu^{2,3,4}, Zhongxuan Luo^{2,3}
and Xin Fan^{2,3*}

¹ School of Software Technology, Dalian University of Technology, Dalian 116024, China.

² DUT-RU International School of Information Science & Engineering, Dalian University of Technology, Dalian 116620, China.

³Key Laboratory for Ubiquitous Network and Service Software of Liaoning Province, Dalian 116620, China.

⁴ Peng Cheng Laboratory, Shenzhen, 518000, China.

*Corresponding author(s). E-mail(s): xin.fan@dlut.edu.cn;

Contributing authors: atlantis918@hotmail.com; linrunja@gmail.com;
rollingplanko@gamil.com; rslu@dlut.edu.cn; zxluo@dlut.edu.cn;

Abstract

Infrared and visible image fusion targets to provide an informative image by combining complementary information from different sensors. Existing learning-based fusion approaches attempt to construct various loss functions to preserve complementary features from both modalities, while neglecting to discover the inter-relationship between the two modalities, leading to redundant or even invalid information on the fusion results. Moreover, most of them focus on strengthening the network with an increase of depth while neglecting the importance of feature transmission, causing vital information degeneration. To alleviate these issues, we propose a coupled contrastive learning network, dubbed CoCoNet, to realize infrared and visible image fusion in an end-to-end manner. Concretely, to simultaneously retain typical features from both modalities and remove unwanted information emerging on the fused result, we develop a coupled contrastive constraint in our loss function. In a fused image, its foreground target / background detail part is pulled close to the infrared / visible source and pushed far away from the visible / infrared source in the representation space. We further exploit image characteristics to provide data-sensitive weights, which allows our loss function to build a more reliable relationship with source images. Furthermore, to learn rich hierarchical feature representation and comprehensively transfer features in the fusion process, a multi-level attention module is established. In addition, we also apply the proposed CoCoNet on medical image fusion of different types, e.g., magnetic resonance image and positron emission tomography image, magnetic resonance image and single photon emission computed tomography image. Extensive experiments demonstrate that our method achieves the state-of-the-art (SOTA) performance under both subjective and objective evaluation, especially in preserving prominent targets and recovering vital textural details. The source code is available at <https://github.com/runjia0124/CoCoNet>.

Keywords: image fusion, infrared and visible image, unsupervised learning, contrastive learning

1 Introduction

Multi-sensor images can acquire complementary and comprehensive information from the same scene for better visual understanding and scene perception, which breaks through the limitations of single sensor imaging [Li et al \(2018b\)](#). By combining the important information from different sensors, a composite image is generated for follow-up image processing or decision-making. In particular, infrared and visible image fusion (IVIF) is an indispensable branch that plays a irreplaceable role in computer vision community. The generating fused results have been widely used for the subsequent applications, including object detection [Wong et al \(2017\)](#), pedestrian re-identification [Duan et al \(2017\)](#), semantic segmentation [Pu et al \(2018\)](#), and image stitching [Jiang et al \(2022\)](#).

Visible sensors imaging by reflecting lights to provide high spatial resolution background details. However, the targets cannot be seen clearly caused by poor lighting or camouflage conditions. In contrast, infrared sensors imaging by discriminative thermal radiation emitted from objects, which are free for challenging conditions and work all day and night. Therefore, it is worthwhile to fuse the infrared and visible image into a single image that simultaneously retain the vital information for both sides.

In the past few years, a large number of approaches for realizing IVIF have been proposed. According to their corresponding adopted theories, these methods can be divided into five categories, including multi-scale transform based methods [Li et al \(2013\)](#), sparse representation based methods [Zhang et al \(2013, 2018\)](#), subspace decomposition based methods [Lu et al \(2014\)](#), hybrid-based methods [Ma et al \(2017\)](#); [Liu et al \(2015\)](#), optimization model based methods [Ma et al \(2016\)](#); [Zhao et al \(2020b\)](#) and others. Some of these methods are dedicated to designing various feature transforms to learn better feature representation [Li et al \(2013\)](#); [Yan et al \(2015\)](#). The others are attempt to discover appropriate fusion rules [Ma et al \(2017\)](#); [Zhang et al \(2018\)](#). However, these methods rely on hand-craft ways and typically have to be time consuming.

Recently, researchers introduced convolutional neural networks (CNNs) to the field of IVIF, with state-of-the-art performance [Li and Wu \(2018\)](#);

[Li et al \(2018a\)](#); [Ma et al \(2019b\)](#); [Xu et al \(2019\)](#). Generally, the deep learning-based methods can be divided into three categories, *i.e.*, auto-encoder-based methods [Li and Wu \(2018\)](#); [Liu et al \(2021a\)](#); [Zhao et al \(2020a\)](#), end-to-end CNN-based methods [Li et al \(2021\)](#); [Xu et al \(2020\)](#); [Zhang et al \(2020a\)](#) and generative adversarial [Ma et al \(2019b, 2020b\)](#) network-based methods.

These existing learning-based methods have achieved outstanding performance, but there are still several issues to solve. First, utilizing CNNs in the IVIF is challenging due to the lack of labeled fused images for supervised learning. Existing approaches attempt to solve it by designing various loss functions to penalize differences between input images and fused results, which may cause massive redundant information to emerge on the fused result [Zhao et al \(2020a\)](#). Second, to achieve outstanding fusion results, existing approaches rely on adjusting trade-off parameters in their loss functions, which causes limited fusion performance and redundant manual work [Li and Wu \(2018\)](#); [Zhang et al \(2020a\)](#). Third, existing learning-based methods are dedicated to introducing skip connections to reduce gradient disappearance and feature degradation during the fusion process. However, the fused results still suffered vital information lose [Liu et al \(2021a\)](#).

In this paper, to address the issues mentioned above, we propose a coupled constative learning network with multi-level feature ensemble for fusing the infrared and visible image in an end-to-end manner, termed as CoCoNet. First, we develop a coupled contrastive learning scheme to maintain the most information from the two modality images, *i.e.*, distinct target of the infrared image and textural details of the visible image. Third, a measuring mechanism is applied to compute the proportional importance of source images for generating data-driven weights. Afterward, these generated weights are applied in our loss function to replace the manually-craft trade-off parameters. Under these specific designs, our CoCoNet can generate a fused result with distinct thermal targets and vivid details. In addition, a multi-level attention module is designed to learn rich hierarchical feature representation and ensure these features have been fully utilized. Last but not the least, our CoCoNet is able to generalized for fusing

the different types of medical images, *e.g.*, magnetic resonance image (MRI) and single photon emission computed tomography (SPECT) image, which retains anatomical information from MRI image and functional information from SPECT image simultaneously. The main contribution of our method are three-folds :

- Considering the major cornerstone in IVIF as maintaining the most important information and removing redundant information from two modality images, we propose coupled contrastive constraints to achieve this goal and couple it seamlessly in the loss function.
- We raise a data-driven mechanism to calculate the information retention degrees to boost intensity and detail consistency between the source images and fused results. This mechanism reduces intensive manually-crafted parameters in the loss function and further boosts fusion performance.
- By designing a multi-level attention module (MAM), our network is able to learn rich hierarchical features representation and effectively avoid feature degeneration during the fusion process.

Extensive qualitative and quantitative experiments on two datasets demonstrate the superiority of our method, outperforming nine state-of-the-art IVIF methods by a large margin. Besides, CoCoNet is able to extend to fuse the medical images with achieving superior performance.

2 Related Works

In this section, we briefly overview the traditional-based fusion methods and deep learning-based ones. Furthermore, the utilization of attention mechanism and contrastive learning in deep learning are also given in following.

2.1 Multi-Modality Image Fusion Methods

2.1.1 Infrared and Visible Image Fusion

Traditional Fusion Methods

In the past few decades, extensive traditional infrared and visible image fusion have been proposed and applied well. Generally, according to

their corresponding adopted theories, all of these traditional-based methods can be divided into six representative categories, *i.e.*, multi-scale transform (MST)-based methods Li *et al.* (2013); Ma *et al.* (2017), sparse representation (SR)-based methods Cui *et al.* (2015); Zhang *et al.* (2018), saliency-based methods Ma *et al.* (2017), subspace-based methods, model-based methods Zhao *et al.* (2018); Liu *et al.* (2021); Zhao *et al.* (2020b), hybrid models and other methods Gangapure *et al.* (2017).

MST are widely used in the field of IVIF, with achieving outstanding fusion performance. These MST-methods target to design various transformation tools, *e.g.*, wavelet transform Petrovic and Xydeas (2004); Lewis *et al.* (2007), non-subsampled contourlet transform Bhatnagar *et al.* (2013), contourlet transform Da Cunha *et al.* (2006), edge-preserving filter based transform Ma *et al.* (2017), and Retinex theory-based transform, to extract features at different scales. Then these transformed features are merged by specific fusion rules. Finally, the fused results are provided by reverse their adopted transforms. Li *et al.* Li *et al.* (2013) applied a guided filter in dealing IVIF task, which provides the visual-pleasant fused results with less noise interference. To preserve abundant details on the fused results, Meng *et al.* Meng *et al.* (2017) introduced an IVIF method was based on the NSCT and object region detection.

Different from MST-based fusion methods with prefixed basis functions, SR-based methods Yin *et al.* (2017); Kim *et al.* (2016); Zhang *et al.* (2018) targets to construct an over-complete dictionary from high-quality natural images. The learned dictionary can sparsely represent the infrared and visible images, thus potentially enhancing the representation of the final fused results. For instance, Kim *et al.* Kim *et al.* (2016) proposed a method that was based on patch clustering, which achieves appealing fusion performance and removes the redundancy of the learned dictionary.

Saliency targets to calculate the significant pixel than neighbours, which attracts visual attention under a bottom-up manner. To this end, researchers have adopted saliency methods to the IVIF task. Ma *et al.* Ma *et al.* (2017) designed a rolling guided filter to decompose the source images into the base and detail layer. Then they used the visual saliency map and weighted least

square optimization to merge the base layer and detail layer, respectively.

The core idea of subspace-based methods is to project high-dimensional source images into low-dimensional subspaces, which is easy to capture the intrinsic structures. Principal Component Analysis (PCA) [Abdi and Williams \(2010\)](#), Independent component analysis (ICA) [Hyvärinen and Oja \(2000\)](#), and Intensity-Hue-Saturation (IHS) [Tu et al \(2004\)](#) are in this category. [Bavirisetti et al. Bavirisetti \(2017\)](#) used fourth-order partial differential equations to decompose image, and then merge the decomposed detail information by PCA. Thus, the abundant can be transferred to the fusion results.

Model-based methods also shed new light on IVIF [Ma et al \(2016\)](#); [Liu et al \(2021\)](#). Based on total variation, [Ma et al. Ma et al \(2016\)](#) first introduced a method for IVIF, which kept the intensity information of infrared images and retained the detailed information of visible images simultaneously. More recently, [Liu et al. Liu et al \(2021\)](#) proposed a bilevel optimization-based method to solve the IVIF and medical image fusion. In addition, the data-driven weight is employed in the model to replace the hand-craft parameters and further boost the fusion performance.

The aforementioned IVIF methods all have two sides, and it is worthwhile to combine their advantages to improve the fusion performance. To this end, [Liu et al. Liu et al \(2015\)](#) introduced a unified fusion framework by combining MST and improved SR; the MST is employed to decompose the source images, and the SR is utilized to obtain fusion coefficients.

Although these traditional-based methods play their roles to the IVIF task with achieving meaningful performance. However, the hand-craft feature extractors and manually designed fusion rules make these traditional-based methods more and more complex, resulting in time-consuming and limited fusion performance for various scenes.

Deep Learning-Based Fusion Methods

Deep learning technique has achieve significant advances in tremendous fusion tasks [Li and Wu \(2018\)](#); [Liu et al \(2021\)](#); [Ma et al \(2019b\)](#); [Liu et al \(2021a\)](#); [Xu et al \(2020\)](#); [Li et al \(2021\)](#); [Ma et al \(2020b\)](#); [Liu et al \(2022b\)](#); [Zhao et al \(2020a\)](#); [Ma et al \(2022b\)](#); [Liu et al \(2022c\)](#), due to its strong non-linear fitting ability from massive data.

Early IVIF methods only employed deep learning for feature extraction or generating weight maps. For instance, [Liu et al. Liu et al \(2021\)](#) adopted two pre-trained CNN to generate two weight maps for merging the base and detail layer, respectively. However, the whole process is still under a traditional optimization model, which limits the fusion performance.

Recently, a part of learning-based methods [Li and Wu \(2018\)](#); [Liu et al \(2021a\)](#); [Zhao et al \(2020a\)](#); [Li et al \(2021\)](#) that utilizing auto-encoder architecture have been proposed. The pre-trained auto-encoder are employed to realize feature extraction and feature reconstruction, in which the fusion rules are fulfilled by manually-designed. [Li and Wu](#) first introduce a auto-encoder network for IVIF. By integrating a dense block in the encoder part, the feature can be extracted comprehensively. Then they used addition and $l1$ -norm rule in the fusion layer to generate fused results. Considering the vital information often degenerate from the network, [Liu et al. Liu et al \(2021a\)](#) employed different reception dilated convolutions to extract feature from a multi-scale prospective, and then merged these extract features by the edge attention mechanism. More recently, [Zhao et al. Zhao et al \(2020a\)](#) proposed an auto-encoder based fusion network, in which the encoder decomposes an image into background and detail feature maps with low-/high-frequency information, respectively. Then the fused result is generated by via the decoder part.

Apart from that, extensive generative adversarial network (GAN)-based fusion methods [Ma et al \(2019b, 2020a,b\)](#) have been proposed, due to its powerful unsupervised distribution estimation ability. For the first time, [Ma et al. Ma et al \(2019b\)](#) established an adversarial game between the visible image and fused result to enhance the textural details. However, they only used the information from the visible image, thus losing contrast or contour of the target on the fused result. To ameliorate this issue, they later introduce a dual discriminators GAN [Ma et al \(2020a\)](#), in which both infrared and visible images are participate in the network, thus significantly boost the fusion performance. To pursue merge the infrared and visible image more appropriately, [Ma et al. Li et al \(2021\)](#) introduced an end-to-end GAN model that integrates multi-classification constraints.

Last but not the least, a growing number of researchers concentrate on designing the general image fusion network Zhang *et al.* (2020b,a); Xu *et al.* (2020). Zhang *et al.* (2020b) introduce a unify fusion network for realizing various image fusion tasks with high efficiency. The network only need trained on one type of fusion dataset, and adjust the fusion rule to face the other types of fusion tasks. Zhang *et al.* (2021) introduced the idea of squeeze and decomposition into the field of image fusion, combined gradient and intensity information to construct a general loss function, and proposed a general fusion network. To realize multiple fusion tasks into a single model, Xu *et al.* (2020) came up with a novel fusion network, in which overcomes the storage and computation issues or catastrophic forgetting in the training phase.

Recently, transformer Vaswani *et al.* (2017a) has received extensive attention since it was proposed in the field of natural language processing. Later, Dosovitskiy *et al.* (2020) proposed the Vision Transformer (ViT) for image classification. This successful examples in other areas of computer vision have inspired the extensive development of transformer based methods in the field of image fusion.

Vibashan *et al.* (2021) took the lead in proposing an image fusion transformer model that can simultaneously use local information and long-range information, which makes up for the lack of the ability of CNN model to extract global context information. Transformer more effectively fuses complementary information of different modalities. After the advanced Swin Transformer Liu *et al.* (2021) was proposed, Tang *et al.* (2022a) migrated it to the field of image fusion and proposed a general fusion framework combining cross domain distance learning, which realized more information complementation in the fusion process.

2.1.2 Medical Image Fusion

Similar to IVIF, the existing traditional methods of MIF can be roughly classified into two types: multi-scale transform based and sparse representation based medical image fusion.

MST is also a commonly used mean in the field of medical image fusion. Compared with MST in

IVIF, their processing flow are similar, but different in details. In the medical field, the common multi-scale transformation methods usually use different wavelet to transform the domain. Yang *et al.* (2008) used the contourlet domain for medical image fusion, proposed a contrast measurement method based on the characteristics of the contour wave to select the part suitable for the human visual system, and further improved the quality of the fused image by combining various fusion rules.

In the field of sparse representation on medical images, Liu *et al.* (2015) proposed an adaptive sparse representation model, which discards the redundant dictionary to learn a compact sub dictionary. The source image block adaptively selects features from the sub dictionary to achieve the effect of diminishing computing costs and effectively reducing artifacts. Liu *et al.* (2019) integrated morphological principal component analysis and convolutional sparse representation into a unified optimization framework, and realized stable visualization effect.

With the extensive application of deep learning in other image fusion fields, some general fusion frameworks Zhang and Ma (2021); Ma *et al.* (2022a); Xu *et al.* (2020) also integrate medical image fusion as their branch tasks. Xu *et al.* (2021) proposed an unsupervised enhanced medical image fusion network to retain both surface and deep-level constraints information.

2.2 Attention Mechanism in Deep learning

The attention mechanism drives from Natural Language Processing (NLP) Parikh *et al.* (2016) and has been successfully applied in CNN-based computer vision tasks Huang *et al.* (2019); Vaswani *et al.* (2017b), *e.g.*, saliency object detection Zhang *et al.* (2021b), semantic segmentation Huang *et al.* (2019); Li *et al.* (2019), image enhancement Lv *et al.* (2019) and image restoration Zhang *et al.* (2019). The attention mechanism is explained by the human biological visual system that allow human to capture ROI (region of interest) information and ignore other unimportant ones more easier.

To explore salient information in both foreground and background regions, Zhang *et*

al. Zhang et al (2021b) introduced a Bilateral Attention Network (BiANet) for the RGB-D saliency object detection task, in which complementary attention mechanism can coordinate refine the uncertain details between foreground/background regions. Liu *et al.* Liu et al (2021b) proposed a hierarchical attention-guided module for multi-exposure image fusion, which allows the network can capture the most important information in extremely exposure regions.

2.3 Contrastive Learning

Contrastive Learning has been obtained comprehensive attention in the self-supervised learning area He et al (2020); Henaff (2020). Compared with other techniques that employ a fixed target, contrastive learning aims to maximizes the mutual features by employing the positive pairs and negative pairs. More precisely, the learned anchor needs pulling the data close to positive samples while pushing it far away from negative ones. Previous works applied contrastive learning into both high-level and low-level computer vision tasks He et al (2020); Wu et al (2021); Xie et al (2021), *e.g.*, object detection Xie et al (2021), image dehazing Wu et al (2021) and image super-resolution Zhang et al (2021a), with achieving SOTA performance. However, there are still few works to apply contrastive learning into the field of infrared and visible image. To this end, we show the flexible of contrastive constraints to perform multi-modality contrast in against to the infrared and visible image, respectively.

3 The Proposed Method

In this section, we first describe the motivation of our CoCoNet, and then introduce the designed loss function, especially for coupled contrastive constraint and self-adaptive learning weight. Besides, the detailed design of the network architecture and multi-level feature ensemble strategy are presented. At the end of this section, we extend our CoCoNet to medical image fusion.

3.1 Motivation

As aforementioned above, the goal of IVIF is to preserve complementary information and remove redundant information from two modality images.

Currently, most of fusion methods use skip connections for avoiding information lose or feature degeneration. However, these directly skip connections may introduce un-wanted information, resulting in vital information lose or artifacts on their fused results. In addition, for the fused image, we expect the foreground target are more closed the infrared image and the background details are more closed to the visible image, respectively. However, the targets/details on the fused result often contain unwanted or redundant information. The contrastive learning achieve great success in computer vision community, which to maximizes the mutual features by employing the positive pairs and negative pairs. Unfortunately, it lacks a contrastive learning based-methods for the field of infrared and visible image fusion. Last but not the least, the hand-crafted trade-off parameters in the loss function are difficult to adjust, which pose a latent threat to the fusion performance.

Consequently, we introduce a coupled contrastive learning network to fill in the gaps of IVIF. A multi-level attention module is designed to learn comprehensive feature representation and then integrate this module in skip connection to avoid feature degeneration during the fusion process. By elaborating construct coupled contrastive constraints with self-adaptive weights in the loss function, we can provide a visual-friendly fused result with distinct foreground thermal target and background faithful details.

3.2 The Proposed CoCoNet

3.2.1 Coupled Constrative Learning

Inspired by previous work on contrastive learning, we propose a coupled contrastive regularization for IVIF, based on two pairs of constraints, *i.e.*, target constraint and detail constraint. Different from supervised learning with explicit guidance of reference images, there are no clear indications of positive and negative samples for infrared and visible image fusion. Hence, the core of applying contrastive learning lies in how to construct positive and negative pairs. In this paper, we argue that the desirable features served as positive and negative samples are included in source images. Concretely, for an infrared image, its foreground salient thermal target is of interest while the rest

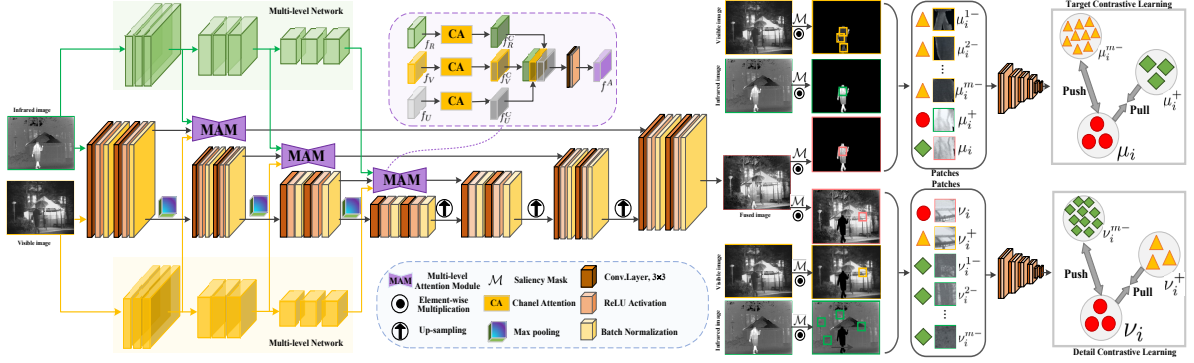


Fig. 1: The overall architecture of our CoCoNet.

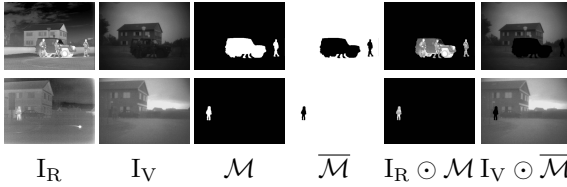


Fig. 2: Typical examples of the salient mask \mathcal{M} in TNO dataset.

parts should be discarded. Similarly, in a visible image, the background vivid textural details is highly demanded while the dark foreground part is less desirable.

For a fused result, we target to achieve two objectives based on two groups of constraints: to improve the saliency of foreground objects, the corresponded targets from the infrared image is utilized as positive samples while the corresponded regions from the visible image is utilized as negative samples. At the same time, in the case we want to preserve the vivid background details on the fused result, we set the visible image as positive while infrared image as negative samples.

In order to introduce artificial prior knowledge to maximize the above objectives, we manually generated masks for corresponding image pairs based on typical infrared images captured in TNO dataset. Specifically, as shown in sFig 2, let \mathcal{M} denote the salient mask of foreground and $\overline{\mathcal{M}}$ represents the salient mask of background ($\overline{\mathcal{M}} = 1 - \mathcal{M}$). For a fused result, we aim to contain more information of foreground objects from the infrared image instead of the same region from the visible image.

To this end, the positive and negative samples for improving foreground saliency, which we

call target constraint, should be $I_R \odot \mathcal{M}$ and $I_V \odot \overline{\mathcal{M}}$. For the latent feature space, we select the commonly used VGG-19 [Simonyan and Zisserman \(2014\)](#), denoted as G , with pre-trained weights. We formulate the loss function of this goal as follows:

$$\mathcal{L}_{ir} = \sum_{i=1}^N w_i \frac{\|\mu_i - \mu_i^+\|_1}{\sum_m^M \|\mu_i - \mu_i^{m-}\|_1}, \quad (1)$$

where N and M are the number of VGG layers and negative samples for each positive sample, respectively. μ_i denotes the foreground feature of the fused image, which is defined as $G_i(I_F \odot \mathcal{M})$. μ_i^+ and μ_i^{m-} are the positive and negative samples, formulated as $\mu_i^+ = G_i(I_R \odot \mathcal{M})$, $\mu_i^{m-} = G_i(I_V^m \odot \overline{\mathcal{M}})$, respectively. m means the m th negative sample. $\|\cdot\|_1$ denotes the ℓ_1 norm.

Likewise, for the background part, we hope to retain more vivid details from visible images, treating background of the infrared image as negative samples, while the visible image background as positive samples. Therefore, the object function for detail constraint can be given as:

$$\mathcal{L}_{vis} = \sum_{i=1}^N w_i \frac{\|\nu_i - \nu_i^+\|_1}{\sum_m^M \|\nu_i - \nu_i^{m-}\|_1}, \quad (2)$$

where ν_i denotes the foreground feature of the fused image, which is defined as $G_i(I_F \odot \overline{\mathcal{M}})$. ν_i^+ and ν_i^{m-} are the positive and negative samples, formulated as $\nu_i^+ = G_i(I_R \odot \overline{\mathcal{M}})$, $\nu_i^{m-} = G_i(I_V^m \odot \mathcal{M})$, respectively. m means the m th negative sample.

3.2.2 Self-adaptive Learning Weight

Image fusion targets to provide an information-abundant image with sufficient details and balanced intensities by combining favorable features of source images. For the infrared and visible fusion task, we learn to minimize the similarity of source images and the fused image. The loss function is mainly composed of two parts, *i.e.*, the structure similarity loss and the intensity similarity loss, which can be define as:

$$\mathcal{L}_{\mathcal{P}} = \alpha\mathcal{L}_{\mathcal{S}} + \mathcal{L}_{\mathcal{N}}, \quad (3)$$

where α is a tuning parameter, $\mathcal{L}_{\mathcal{S}}$ and $\mathcal{L}_{\mathcal{N}}$ denote structure similarity loss and intensity similarity loss. $\mathcal{L}_{\mathcal{S}}$ is measured by the structure similarity index measure (SSIM) Wang et al (2004), which is widely used to indicate the difference of images based on similarities of contrast, light, and structure. It is given as follows:

$$\mathcal{L}_{\mathcal{S}} = \sigma^a(1 - \mathcal{S}(\mathbf{I}_V, \mathbf{I}_F)) + \sigma^b(1 - \mathcal{S}(\mathbf{I}_R, \mathbf{I}_F)), \quad (4)$$

where $\mathcal{S}(\cdot)$ denotes SSIM value.

$\mathcal{L}_{\mathcal{N}}$ is adopted to strengthen the constraints on the differences of intensity distributions, formulated as:

$$\mathcal{L}_{\mathcal{N}} = \gamma^a \|\mathbf{I}_V - \mathbf{I}_F\|_2 + \gamma^b \|\mathbf{I}_R - \mathbf{I}_F\|_2, \quad (5)$$

where $\|\cdot\|_2$ is Mean Square Error (MSE).

In Equation 4 and Equation 5, σ and γ are two pairs of proportional weights that balances the proportion of the visible image and infrared image. σ and γ consists of $\{\sigma^a, \sigma^b\}$ and $\{\gamma^a, \gamma^b\}$, respectively. They are empirically set to fixed values in existing methods Zhang et al (2020a). However, a fixed manner is incapable to make full use of the distinctive details. Therefore, our method takes the best advantage of data characteristics to achieve a self-adaptive loss function by optimizing the image-specific weights σ and γ .

For one thing, we expect the fused image to retain abundant information (*e.g.*, substantial details). Thus, Average Gradient (AG) is applied to optimize the weight parameter σ by maximizing the value of the following equation:

$$\text{AG} = \frac{1}{HW} (\|\nabla_h \mathbf{I}_F\|_1 + \|\nabla_v \mathbf{I}_F\|_1), \quad (6)$$

where the $\nabla_h \mathbf{I}_F$ and $\nabla_v \mathbf{I}_F$ represent the first-order differential of the fused image from horizontal and vertical direction, respectively. H and W are the height and width. $\|\cdot\|_1$ denotes ℓ_1 norm.

For another, to fuse images with high contrast and clear edges, image Entropy (EN) is employed to update weight parameter γ . EN is formulated as follows:

$$\text{EN} = - \sum_{x=0}^{L-1} p_x \log_2 p_x, \quad (7)$$

where L denotes grey level of the given image, p_x is the probability that a pixel lies in the corresponding grey level.

Consequently, combining all the restrictions above, we give the following loss function to guide our learning:

$$\mathcal{L}_{total} = \mathcal{L}_{\mathcal{P}} + \mathcal{L}_{ir} + \mathcal{L}_{vis}, \quad (8)$$

where $\mathcal{L}_{\mathcal{P}}$ is the self-adaptive loss, and \mathcal{L}_{ir} and \mathcal{L}_{vis} are the two pairs of contrastive loss respectively.

3.3 Network Architecture

As shown in Figure 1, each convolution block consists of two groups of 3×3 convolutional lays followed by batch normalization and LeakyReLU. The feature maps from each depth layers can be represented as: f_{U0} , f_{U1} , f_{U2} , f_{U3} from layers with 32, 64, 128, 512 channels respectively. For the multi-level attention module, we select two VGG19 with pre-trained weights as our backbone. It takes the visible image and infrared image as inputs in a separate manner, as an attempt to make full use of high level features of the source image. Infrared features obtained from the backbone are denoted as f_{R1} , f_{R2} , f_{R3} , which come from layers of 64, 128 and 256 channels, respectively. Likewise, visible features extracted from the backbone are represented as f_{V1} , f_{V2} , f_{V3} from the corresponding layers.

To employ more high-level features into the fused image, we propose a multi-level attention module (MAM) to achieve comprehensive feature representation from the source images. Meanwhile, we expect this attention to intensify the extracted features by a global enhancement. Based on the obtained features f_U , f_R and f_V above, a

channel attention is first performed:

$$f_U^C = \mathbf{CA}(f_U), f_R^C = \mathbf{CA}(f_R), f_V^C = \mathbf{CA}(f_V), \quad (9)$$

where \mathbf{CA} denotes channel attention, which will be described in the following part. To fuse these features, we apply convolution operations for each group of features:

$$\begin{aligned} f_{A1} &= \mathbf{Conv}(\mathbf{Concate}(f_{U1}^C, f_{R1}^C, f_{V1}^C)) \dots \\ f_{An} &= \mathbf{Conv}(\mathbf{Concate}(f_{Un}^C, f_{Rn}^C, f_{Vn}^C)), \end{aligned} \quad (10)$$

where \mathbf{Conv} represents a convolution layer with 3×3 kernels, and $\mathbf{Concate}$ means concatenation.

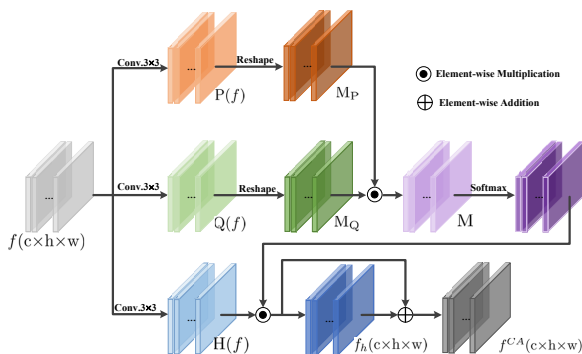


Fig. 3: The architecture of channel attention.

The detail architecture of channel attention is illustrated in Figure 3. Given a feature f of dimension $\mathbb{R}^{C \times H \times W}$, we first use a convolution layer to generate three components $\mathbf{P}(f)$, $\mathbf{Q}(f)$, $\mathbf{H}(f)$, and reshape $\mathbf{P}(f)$, $\mathbf{Q}(f)$ from $\mathbb{R}^{C \times H \times W}$ to $\mathbb{R}^{C \times H \times W}$, obtaining \mathbf{M}_P , \mathbf{M}_Q . Then a matrix multiplication is applied on \mathbf{M}_P and the transpose of \mathbf{M}_Q followed by a softmax layer to compute the attention feature map $\mathbf{M} \in \mathbb{R}^{C \times C}$. Thereafter, a matrix multiplication is performed between the transpose of $\mathbf{H}(f)$ and \mathbf{M} . The result is finally reshaped and added back to the source image \mathbf{H}_f .

3.4 Extension to Medical Image Fusion

In this section, we extend our CoCoNet to fuse the medical images, *e.g.*, MRI and PET image fusion, MRI and SPECT image fusion. The PET and SPECT images are regarded as pseudo-color images. We first transform them to color images,

and then apply CoCoNet to fuse the MRI image and intensity component of PET and SPECT image, respectively.

3.4.1 Medical Image Fusion Background

With the rapid development of clinical requirement, a series of medical imaging technologies, *e.g.*, X-ray, computed tomography (CT), MRI, PET and SPECT, has been introduced in the past few decades. However, each imaging technology has its advantages and limitations. For instance, X-ray is an electromagnetic wave with extremely high frequency, short wavelength, and high energy, which has strong penetrability. It has been widely used in fluoroscopy before diagnosis or surgery. Compared with the conventional X-ray photography, CT can provide detect the slight difference of the bone density with high resolution, but it has limitation in representing tissue characterization. Apart from that, MRI can not only display the morphological structure of the organizational organs, but also display the functional conditions and biochemical information of certain organs. However, MRI lacks of the description of the soft tissue activity. In contrast, both PET and SPECT are functional imaging, which present the difference in the intensity of the human tissue activity according to the difference in the concentration of the aggregation. Evidently, each imaging modality unavoidably has its respected characteristics and inherent drawbacks. It is worthwhile to combine the advantages from different modality images and then provide an informative and complementary fused image for the clinical diagnosis.

In past few years, a series of hybrid imaging technologies, *e.g.*, CT-MRI, MRI-PET and MRI-SPECT, have been introduced in our daily life. In this paper, we take two typical medical image fusion, *i.e.*, MRI-PET and MRI-SPECT as an example and apply CoCoNet to solve this issue. As previous paragraph mentioned above, both PET and SPECT images can provide functional and metabolic information, which are widely used for analyzing the functions or metabolic conditions of each organs. These obtained images are rich in color but lack in resolution. In contrast, MRI image can better portray soft tissue structures in organs. Usually, it has high spatial resolution. Therefore, by integrating advantages from each

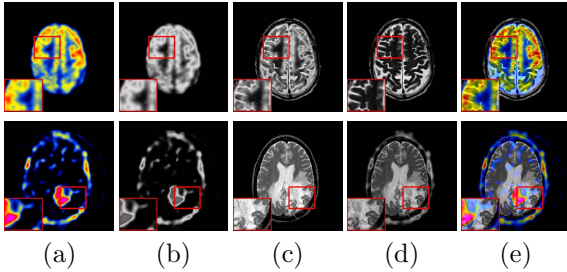


Fig. 4: Schematic illustration of MIF tasks, where (a) pet/spect image, (b) Luminance (Y) channel of pet/spect image, (c) mri image, (d) Luminance channel (Y) of fused image, (e) fused image.

modality image, we can obtain complementary and comprehensive information in a single image.

In most of cases, as shown in Figure 4(a), both PET and SPECT are shown in pseudo-color, in which the color are represented as functional information. For the fused image, the color information should in line with the PET or SPECT images. To this end, we decouple the PET and SPECT image into YCbCr color space with three channels. Then, we employ Y channel (the luminance channel shown in Figure 4(b)) to fuse with the MRI image PET and SPECT use the intensity information of Y channel to represent the feature distribution, which is similar to the infrared image, while MRI image shown in Figure 4(c) has rich texture organization details, which is similar to the visible image. Therefore, MIF and IVIF have similar task objectives, that is, to reduce spatial detail distortion and color intensity distortion of fused images and corresponding modalities. After getting the fused image(Figure 4(d)) by Y channel and MRI images, other two channels are remained unchanged to recover the color information, as shown in Figure 4(e).

3.4.2 CoCoNet for Medical Image

Fusion

Building on the unique characteristics of MRI sequence and functional sequences (i.e., PET and SPECT) mentioned above, we can also apply the proposed coupled contrastive learning to integrate desirable features from different medical modalities. We should first define features of interest in MRI and functional (i.e., PET/SPECT) modalities respectively. MRI sequences are rich in soft tissue structure, which provides clear indications

of the brain skeleton. On the other hand, To better retain salient structure information from the MRI image, and simultaneously fuse functional information which reflects metabolic activity of organs or tissues, as well as the function and distribution of receptors. Therefore, we are able to clarify the useful features from two modalities as salient structure information from the MRI sequence, and functional indications from the functional sequence. Specifically, to combine useful features from both sides, we propose to impose a MRI-segmented mask and its reverse version on the MRI sequence and functional sequence, respectively, for a better constraint on the features we aim to extract. For a fused image, we hope its salient regions to resemble the corresponded MRI image, but less similar to the same region from its functional counterpart. In the same vein, we expect the other regions in the fused image to be closer to the functional sequence, but further from the MRI counterpart in the latent feature space. In fact, a common problem for fusing MRI and functional sequences is that the texture details in MRIs tend to get covered, thus weakened, after fusing with its functional counterpart. To partially alleviate this issue, our salient masks are first generated by segmenting the MRI image following the research of Li *et al.* Li and Chi (2005), denoted as $\mathcal{M}_m = \mathcal{M}$. We expect the fused image to resemble the MRI sequence under regions masked by \mathcal{M}_m , for reserving soft tissue textures. At the same time, according to contrastive learning, the functional sequence in the same region serves as negative samples, which aid to stress MRI features. This process can be described as follows:

$$\mathcal{L}_{mri} = \sum_{i=1}^N w_i \frac{\|\mu_i - \mu_i^+\|_1}{\sum_m^M \|\mu_i - \mu_i^{m-}\|_1}, \quad (11)$$

where N and M are the number of VGG layers and negative samples for each positive sample, respectively. μ_i denotes the MRI structure feature of the fused image, which is defined as $G_i(I_F \odot \mathcal{M}_m)$. μ_i^+ and μ_i^{m-} are the positive and negative samples, formulated as $\mu_i^+ = G_i(I_{MRI} \odot \mathcal{M}_m)$, $\mu_i^{m-} = G_i(I_{Fun}^m \odot \mathcal{M}_m)$, respectively. Superscript m means the m th negative sample. $\|\cdot\|_1$ denotes the ℓ_1 norm.

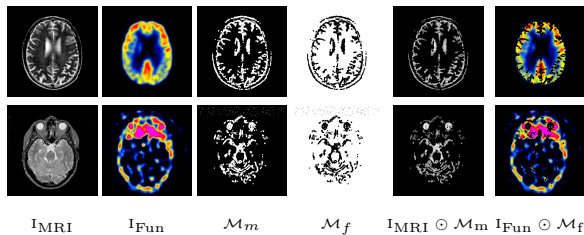


Fig. 5: Typical examples of the segmentation mask on medical image fusion task.

On the contrary, the functional sequence can provide abundant intensity information of the subject’s functional activities, e.g., blood flow. To retain most favorable features from functional sequences, we first reverse the MRI-segmented mask \mathcal{M}_m to get $\mathcal{M}_f = 1 - \mathcal{M}_m$. Then \mathcal{M}_f is imposed on a functional sequence to extract most informative features, which include metabolic information of a subject. Regions of the fused image under mask \mathcal{M}_f should be consistent with the functional image, while less similar to the MRI image. This whole process can be modeled using a twin contrastive learning-based loss function given as follows:

$$\mathcal{L}_{fun} = \sum_{i=1}^N w_i \frac{\|\nu_i - \nu_i^+\|_1}{\sum_m^M \|\nu_i - \nu_i^{m-}\|_1}, \quad (12)$$

where ν_i denotes the functional features of the fused image, which is defined as $G_i(I_F \odot \mathcal{M}_f)$. ν_i^+ and ν_i^{m-} are the positive and negative samples, formulated as $\nu_i^+ = G_i(I_{Fun} \odot \mathcal{M}_f)$, $\nu_i^{m-} = G_i(I_{MRI}^m \odot \mathcal{M}_f)$, respectively. Superscript m means the m th negative sample.

4 Experiments

4.1 Experimental Settings

4.1.1 Datasets

The infrared and visible image pairs we utilize to evaluate our method are collected from the TNO ¹ and the RoadScene Xu et al (2020), which are publicly available. The above mentioned datasets are clarified below.

TNO dataset The TNO is a widely used dataset for infrared and visible image fusion. We adopt TNO as the benchmark to train our network for its high quality images with distinctive scenarios. **RoadScene dataset** The RoadScene includes realistic driving scenes (e.g., vehicles, pedestrians and road symbol signs). It contains 221 representative image pairs with no uniform resolution, collected from authentic driving videos.

4.1.2 Training details

Our entire fusion framework is trained on the TNO dataset through two phases: training and fine-tuning.

In the training stage, We first select 46 pairs of images and convert them to greyscale ones. To make full use of the gradient and entropy of each image in the proposed self-adaptive training, we crop 1410 patches of size 64×64 from them. Then, the training patches are normalized to $[-1, 1]$ and fed into our network. We apply Adam as the optimizer and set the learning rate to 0.0001. The batch size is 10 and the epoch in this phase is 10.

In the fine-tuning phase, we adopt 18 images with salient masks from TNO, and crop them into 1410 images of size 64×64 in the training stage. For the contrastive learning, we use one positive sample with three negative samples (one corresponded with the positive patch and two randomly picked up from other negative patches). The network is fine-tuned for 5 epochs, the optimizer, learning rate and batch size settings are the same as that in the training phase. The tuning parameter α is set to an empirical value of 20.

Similarly, to train our model for medical imaging, two stages are required: training and finetuning. 2662 PET patches and 4114 SPECT patches images are selected from Atlas² dataset for training and finetuning. All images are cropped to size 64×64 and normalized to $[-1, 1]$ as training set. We select Adam as the optimizer and learning rate is set to 0.0001 in both stages. In the training stage, the model is trained for 3 epochs with batch size of 30. In the finetuning stage, the model is trained for 1 epoch with batch size of 10. The contrastive learning setting is the same as the IVIF task, with a single positive sample and 3 negative samples for each image. The tuning parameter α is set to 20.

¹[https://figshare.com/articles/TNO Dataset/1008029](https://figshare.com/articles/TNO_Dataset/1008029) Image Fusion

²<http://www.med.harvard.edu/aanlib>

4.1.3 Evaluation metrics

To quantitatively evaluate the fusion performance, in this letter, we select six commonly used metrics for image quality measurement, including EN Roberts et al (2008), AG Eskicioglu and Fisher (1995), SF Eskicioglu and Fisher (1995), SD Aslantas and Bendes (2015), SCD Ma et al (2019a) and VIF Han et al (2013). Their details are given as follows.

Entropy (EN) EN measures the abundance of information included in an image, a larger value indicates that the fusion strategy performs better. The formulation is given as Eq. 7.

Average gradient (AG) AG measures the gradient information of the fused image, which can reflect the details of the fused image. The formulation is given as Eq. 6.

Spatial frequency (SF) SF is a criterion that reflects the change of gray level in an image. An image with a higher SF value possesses more textural details. It is obtained based on horizontal and vertical gradient information. The mathematical expression can be described as follows:

$$SF = \sqrt{H^2 + V^2} \quad (13)$$

where H and V are:

$$H = \sqrt{\frac{1}{MN} \sum_{i=1}^M \sum_{j=2}^N |I_F(i, j) - I_F(i, j-1)|^2} \quad (14)$$

$$V = \sqrt{\frac{1}{MN} \sum_{i=2}^M \sum_{j=1}^N |I_F(i, j) - I_F(i-1, j)|^2} \quad (15)$$

where M and N are the width and height of the estimated image.

Standard deviation (SD) SD is utilized to measure whether an image has abundant information and high contrast. A larger SD value suggests more characteristics included in an image. It is given as follows:

$$SD = \frac{1}{MN} \sum_{i=1}^M \sum_{j=1}^N |I_F(i, j) - \mu|^2 \quad (16)$$

where μ is the average pixel value, M and N are the width and height of the estimated image.

The sum of the correlations of differences(SCD) SCD is an index based on image correlation. First, the definition of correlation about source image I_X and fused image I_F is given as follows:

$$r(I_X, I_F) = \frac{\sum_{i=1}^M \sum_{j=1}^N (I_X(i, j) - \overline{I_X})(I_F(i, j) - \overline{I_F})}{\sqrt{\sum_{i=1}^M \sum_{j=1}^N (I_X(i, j) - \overline{I_X})^2 (\sum_{i=1}^M \sum_{j=1}^N (I_F(i, j) - \overline{I_F})^2)}} \quad (17)$$

The difference between the fused image and the source images as $D_{V,F}$ and $D_{R,F}$, which correspond the correlation between the source image and the difference image respectively. SCD is defined as follows:

$$SCD = r(I_V, D_{V,F}) + r(I_R, D_{R,F}). \quad (18)$$

Visual information fidelity for fusion (VIF) VIF evaluates image quality based on its fidelity, which determines whether an image is visually-friendly. It assesses the amount of valid information fused from the source image. A larger value indicates better quality. VIF is defined as follows:

$$VIF(I_V, I_R, I_F) = \sum_k p_k \frac{\sum_b FVID_{s,b}(I_V, I_R, I_F)}{\sum_b FVIND_{s,b}(I_V, I_R, I_F)} \quad (19)$$

where $FVID_{s,b}$ is the fusion visual information with distortion, and $FVIND_{s,b}$ denotes the fusion visual information without distortion, in the b th block, s th sub-band.

4.2 Results and Analysis on IVIF

Qualitative Comparisons on TNO In Figure 6, we compare our CoCoNet with several SOTA methods: DenseFuse Li and Wu (2018), FusionGAN Ma et al (2019b), PMGI Zhang et al (2020a), DIDFuse Zhao et al (2020a), GANMcC Ma et al (2020b), RFN Li et al (2021), MFEIF Liu et al (2021a), U2Fusion Xu et al (2020), SwinFusion Ma et al (2022a), SDNet Zhang and Ma (2021), SMOA Liu et al (2021c) and TarDAL Liu et al (2022a) on samples from the TNO dataset, in terms of visual effects. Owing to the proposed contrastive learning, overall, our results render higher contrast and the foreground targets are much brighter (*e.g.*, trees, leaves, and foreground objects

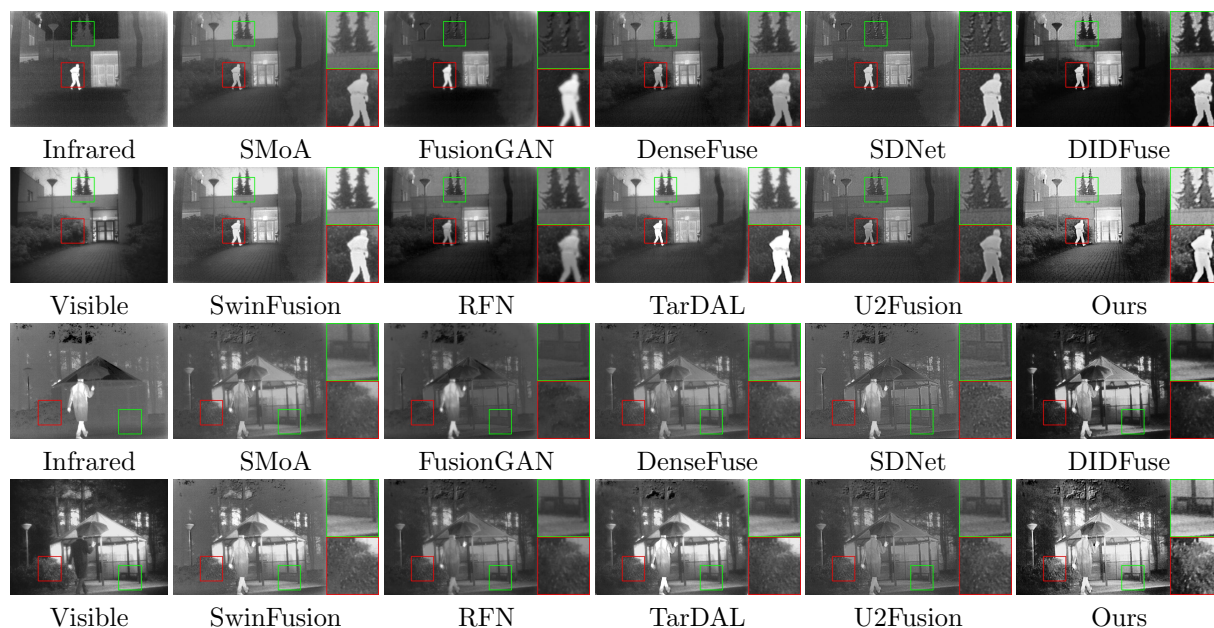


Fig. 6: Visual results comparison between different methods on TNO dataset. Our method is better in preserving detailed textural details and distinctive thermal target, especially in the zoomed-in patches.

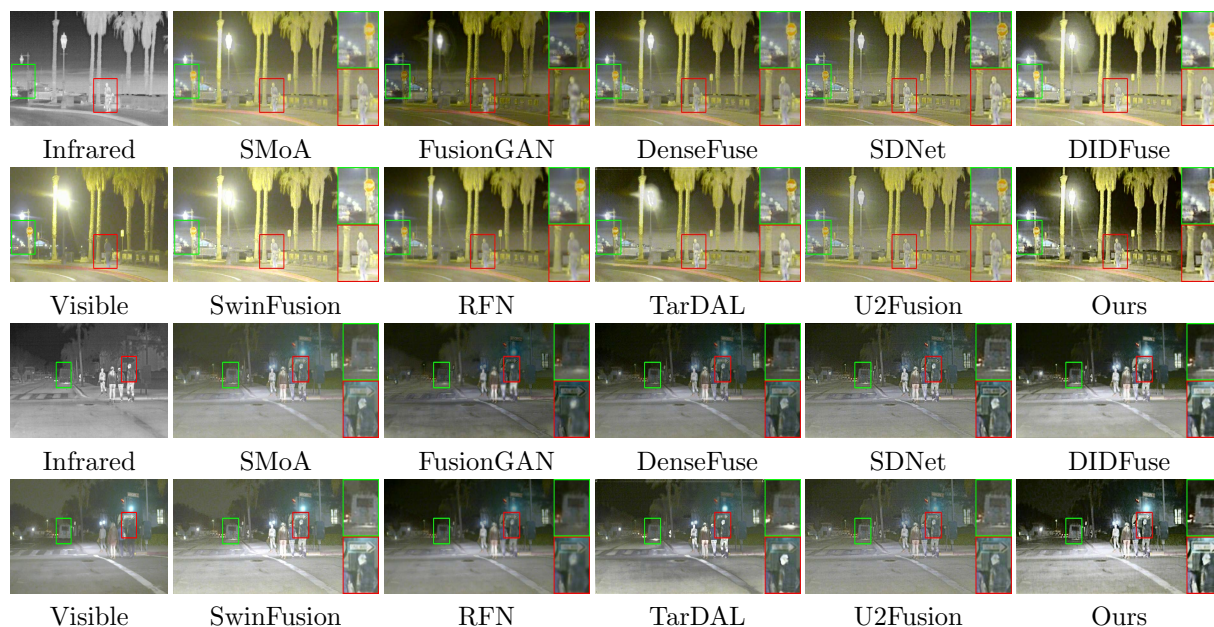


Fig. 7: Visual results comparison between different methods on Roadscene dataset. Our method has advantage in retaining the most information, *e.g.*, the pedestrians in the patches. Best viewed on screen.

Table 1: Quantitative comparisons of fourteen methods on the TNO and RoadScene Datasets.

Method	TNO						RoadScene					
	EN	SD	VIF	SF	AG	SCD	EN	SD	VIF	SF	AG	SCD
DenseFuse	6.961±0.318	9.835±0.914	0.783±0.206	0.0383±0.0127	3.742±1.251	1.726±0.251	7.143±0.262	9.875±0.813	0.808±0.107	0.0384±0.0121	3.815±1.313	1.728±0.149
FusionGAN	6.704±0.335	9.057±1.101	0.608±0.159	0.0289±0.0097	2.764±0.788	1.194±0.546	7.033±0.304	9.994±0.813	0.617±0.077	0.0318±0.0093	3.050±0.979	0.995±0.552
PMGI	7.130±0.204	9.984±0.800	0.829±0.229	0.0371±0.0108	3.725±1.152	1.620±0.381	7.293±0.195	10.139±0.596	0.854±0.097	0.0389±0.0096	3.995±1.113	1.357±0.558
DIDFuse	7.208±0.375	10.200±1.125	0.800±0.184	0.0524±0.0199	4.982±1.950	1.769±0.191	7.355±0.219	10.997±0.659	0.851±0.107	0.0481±0.0155	4.723±1.653	1.766±0.150
GANMcC	6.881±0.337	9.580±0.640	0.676±0.189	0.0265±0.0070	2.719±0.763	1.590±0.324	7.212±0.374	10.025±0.640	0.757±0.081	0.0325±0.0076	3.403±0.942	1.588±0.260
RFN	7.146±0.245	9.946±0.838	0.785±0.188	0.0244±0.0078	2.896±1.063	1.728±0.256	7.306±0.257	9.978±0.763	0.803±0.101	0.0273±0.0078	2.882±1.026	1.773±0.135
MFEIF	6.910±0.444	9.740±1.182	0.788±0.146	0.0327±0.0138	3.291±1.628	1.668±0.232	6.993±0.288	10.008±0.709	0.827±0.100	0.0321±0.0091	3.202±1.038	1.590±0.181
U2Fusion	6.650±0.364	9.524±1.044	0.672±0.147	0.0374±0.0148	3.938±1.660	1.484±0.311	6.990±0.321	9.878±0.813	0.749±0.113	0.0455±0.0165	4.686±1.841	1.381±0.377
SwinFuse	7.015±0.463	9.866±1.117	0.887±0.134	0.0494±0.0229	4.882±2.534	1.623±0.209	6.944±0.357	10.405±0.692	0.849±0.101	0.0414±0.0136	3.872±1.447	1.601±0.199
SDNet	6.890±0.309	9.403±1.171	0.749±0.195	0.0512±0.0182	4.991±1.772	1.493±0.312	7.240±0.246	10.039±0.682	0.806±0.095	0.0516±0.0156	5.199±1.760	1.420±0.305
SMoA	6.782±0.454	9.476±1.187	0.719±0.135	0.0318±0.0130	3.037±1.478	1.603±0.267	6.908±0.297	9.678±0.813	0.765±0.102	0.0315±0.0092	3.124±0.991	1.487±0.239
TarDAL	7.238±0.427	9.929±1.102	0.803±0.119	0.0522±0.0117	4.645±1.415	1.550±0.304	7.210±0.245	10.111±0.784	0.790±0.086	0.0475±0.0068	4.044±0.989	1.339±0.295
Ours	7.776±0.081	10.591±0.477	0.893±0.268	0.0831±0.0280	7.967±2.696	1.794±0.091	7.693±0.094	10.674±0.509	0.854±0.091	0.0718±0.0193	6.537±2.001	1.817±0.051

framed by the red and green boxes). As indicated in the first picture, the salient object (boxed by a red frame) is sharper and clearer, thanks to the infrared contrast and semantic features extracted from multi-level attention. DenseFuse and DIDFuse can also give clear thermal features, however, their images are not bright enough thus causing degradation of the final visual effects. FusionGAN and RFN fail to provide clear targets (the human in their results appear blurry). On the other hand, we can retain vivid textural details from the visible image as well. As displayed in the second compared picture, the red box showcases abundant and clear details of the leaves, while FusionGAN, DIDFuse and SMoA provide nearly no detailed textures. From a comprehensive view, the proposed method obtains the highest quality of both infrared targets and visible features, and fuses both modalities in a natural manner. Although DenseFuse and FusionGAN can also produce relatively desirable foreground targets, they fail to give clear background information, their images tend to be whether dark or blurry. In a word, our CoCoNet achieves the best balance of both saliency and vivid details.

Qualitative Comparisons on RoadScene We also display the visual comparison of our method and the state-of-the-arts on typical realistic driving scenes (*e.g.*, roads, symbol signs and pedestrians) in Figure 7. Generally, all of these methods can fuse the thermal radiation and textural structure details from the source image to some extent. However, RFN and FusionGAN tend to have blur edges. Our method, TarDAL and SDNet all produce visual-friendly fusion images, among which our salient targets (*i.e.*, the pedestrians framed by red boxes) are much brighter and more conspicuous. Unfortunately, RFN fails to combine as much infrared information as other methods, and this causes their objects less clear. On the other hand,

our CoCoNet also achieves the best performance in terms of vivid structure details. In the second compared picture, one can see that the truck indicated by the green box renders much better textures even in a relatively low-light scene. Nevertheless, FusionGAN and PMGI are not able to tackle such problems, they appear dark and fuzzy in the boxed region. We give this credit to the proposed multi-level attention, in which we fuse more high-level features and rearrange the importance of different feature channels. Because of this, our images are sharper and clearer. Although TarDAL can also give good quality fusion result, the output tends to be influenced by the glow, thus degrading the visibility. Overall, we have reached the first class in road scenes and our method is more robust in various scenarios.

Quantitative Comparisons on TNO To give a better view of the performance of CoCoNet, we provide the evaluations of all methods on several important metrics discussed in the above section. The results are shown in Figure 8. It is obvious that on TNO dataset, we achieve the highest results on all six metrics, which demonstrates that the proposed CoCoNet is able to make full use of vital features from the source image. Besides, in Table 1, we also display the average value and standard deviation of each metric, to demonstrate our overall performance. For TNO dataset, it's noticeable that on SF and AG, we show an overwhelming advantage over the second best method, *e.g.*, SwinFuse and DIDFuse by even 58% higher score. This further demonstrates that due to the proposed self-adaptive learning, we are capable of giving images with more grey levels, hence better contrast and details. DIDFuse also performs relatively excellent results in terms of SD and SCD. TarDAL produces satisfying results on EN.

Quantitative Comparisons on RoadScene We can process not only military scenes, but also

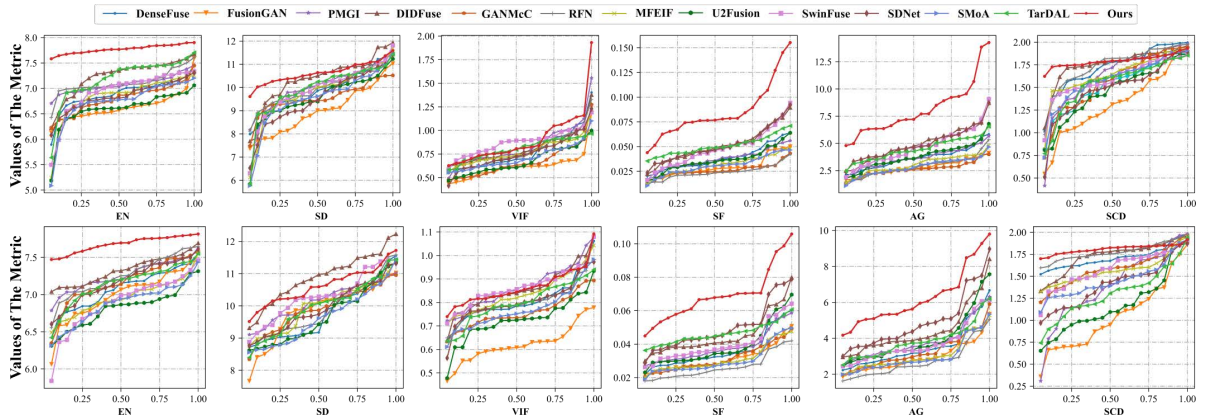


Fig. 8: Quantitative comparisons of five metrics, i.e., EN, SD, VIF, SF, AG and SCD, on 20 image pairs from the TNO dataset (the first row) and other 20 image pairs from the RoadScene dataset (the second row). The thirteen state-of-the-art methods are used for comparison. A single point (x, y) on the curve denotes that there are $(100 \times x)\%$ percent of image pairs that have metric values no more than y .

complex driving scenarios. Thanks to the contrast learning, the fused image contains distinctive grey levels with high contrast. Figure 8 also displays a quantitative comparison evaluated on RoadScene dataset at the second row. Generally, we achieve the best on EN, SF, AG, SCD and VIF and SOTA results on SD. In Table 1, an evaluation of all methods is also listed. This showcases that our method can fuse the best amount of information from source images, and our visibility and sharpness are of the top level as well. It’s worth mentioning that the proposed CoCoNet is 58% higher than the second best SDNet on SF. This indicates much more information with abundant characteristics is included in our results even in complex real scenes, thanks to self-adaptive learning strategy.

4.3 Ablation Study

In this part, we discuss the necessity of different modules in our proposed CoCoNet.

Effectiveness of MAM To ablate the use of multi-level attention mechanism, we remove either features generated by pretrained VGG backbone, channel attention, or both, to generate three variations of the MAM, respectively. In Figure 9, we illustrate these variations along with our full MAM, where (a) removes both channel attention and pretrained VGG backbone, (b) means the absence of pretrained backbone, (c) removes

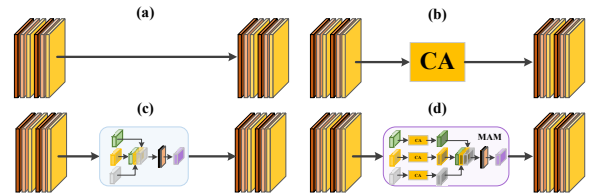


Fig. 9: Visual display of different architectures of MAM, where (a) skip connection only, (b) skip connection with channel attention, (c) skip connection with channel attention and backbone features, (d) our full MAM.

channel attention from MAM and (d) our full MAM.

The numerical results are reported in Table 2, where M1, M2, M3 and M4 are corresponded to the aforementioned (a), (b), (c) and (d), respectively. It’s notable that removing the pretrained VGG features causes a significant drop in metrics on both TNO and RoadScene datasets, which proves the importance of complementary high level features extracted from the pretrained backbone. To prove the importance of channel attention, we also notice a boost of performance from M1 to M2 and M3 to M4 on EN, SF, SD and VIF. This demonstrates that channel attention rearranges the weights of different channels obtained from both modalities, benefiting the overall textural details of the fused image.

Table 2: Quantitative comparisons of different model architectures.

Model	TNO Datasets						Roadscene Dataset					
	EN	SD	VIF	SF	AG	SCD	EN	SD	VIF	SF	AG	SCD
M1	6.564	8.965	0.705	0.0531	4.166	1.736	6.637	9.431	0.698	0.0430	4.31	1.511
M2	6.786	9.288	0.774	0.0596	5.645	1.681	6.839	9.611	0.769	0.0514	5.033	1.524
M3	7.325	9.511	0.823	0.0675	6.536	1.703	7.288	9.980	0.833	0.0591	5.653	1.623
M4	7.776	10.591	0.893	0.0831	7.967	1.794	7.693	10.674	0.854	0.0718	6.537	1.817

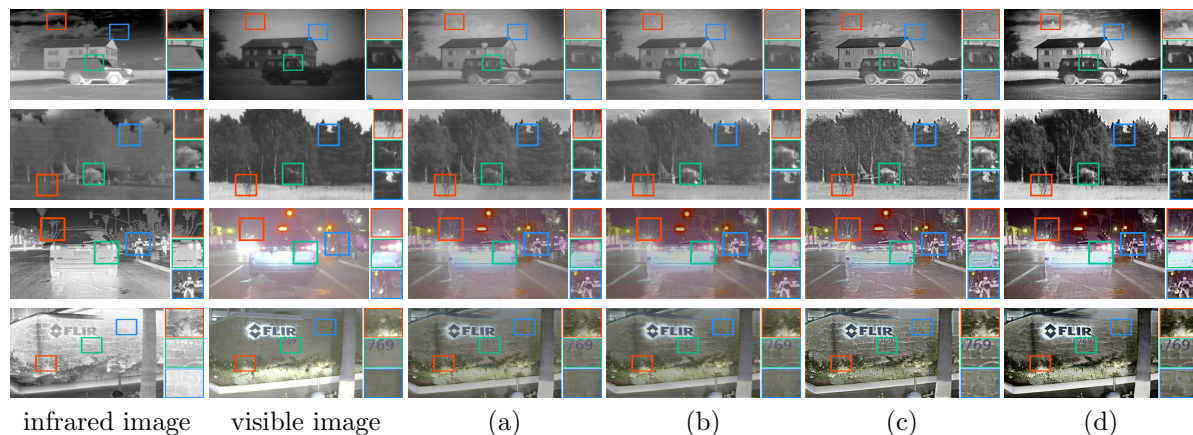


Fig. 10: Visual comparison between different model architectures of the proposed MAM, where (a) skip connection only, (b) skip connection with channel attention, (c) skip connection with channel attention and backbone features, (d) our full MAM. The full MAM is better in preserving informative features, especially in the zoomed-in patches.

Moreover, visual comparisons of M1 to M4 are also provided in Figure 10. It is obvious that by adding the pretrained VGG features, the acuteness of the fused image is greatly improved. Consequently, column (d) and column (c) are much sharper than (b) and (a), *e.g.*, the alphabets indicated by green boxes are clearer in column (c) and (d), and the global structure information is more visual-friendly. By reorganizing feature channels, channel attention enables our network to further remove undesirable noises and retain richer details, which is reflected on the differences between column (c) and (d).

Effectiveness of self-adaptive learning Additional experiments are conducted on TNO and RoadScene datasets to validate the superiority of the proposed self-adaptive learning. In Figure 11, we visualize performance of several training weights designed in a hand-crafted manner and the proposed self-adaptive weights measured

based on internal characteristics of the source image. Specifically, σ and γ are the weights for SSIM and MSE, respectively. We display fused results where several possible fixed weight combinations are adopted (*e.g.*, σ^a ranging from 0 to 1 while making sure the sum of σ^a and σ^b to be 1) to compare with the self-adaptive strategy (presented in the last column). As Figure 11 suggests, the self-adaptive manner achieves much higher contrast, stressing both salient thermal target and vivid details from the visible image by using average gradient and entropy information, as indicated by the green and red boxes. The grass details are clearer with brighter pixels, and the building structure preserves fined edges. Overall, automatically learned weights can generate images with better global contrast.

Besides, we plot quantitative results in Figure 12 to further demonstrate our effectiveness. Results in the first row report the performance

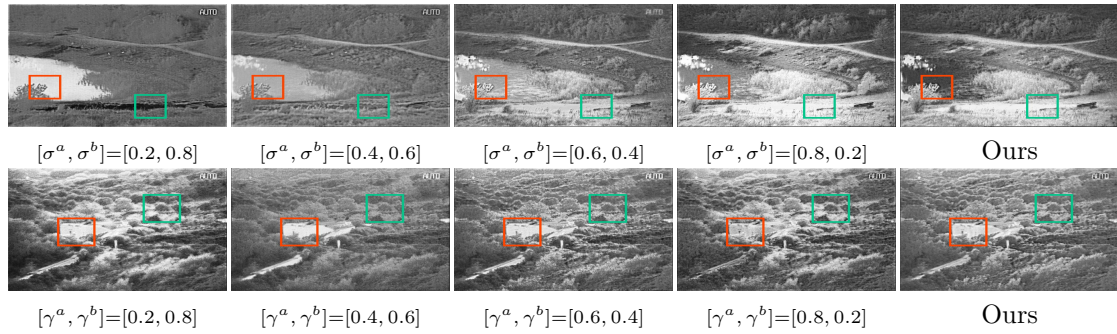


Fig. 11: Visual results comparison among different parameter setting of σ and γ . The top row shows the results with manually-craft σ and the proposed self-adaptive weight, the second row shows the results on γ correspondingly. Note that the self-adaptive weight is better in preserving detailed textural details and considerable contrast, especially in the zoomed-in patches. Best viewed on screen.

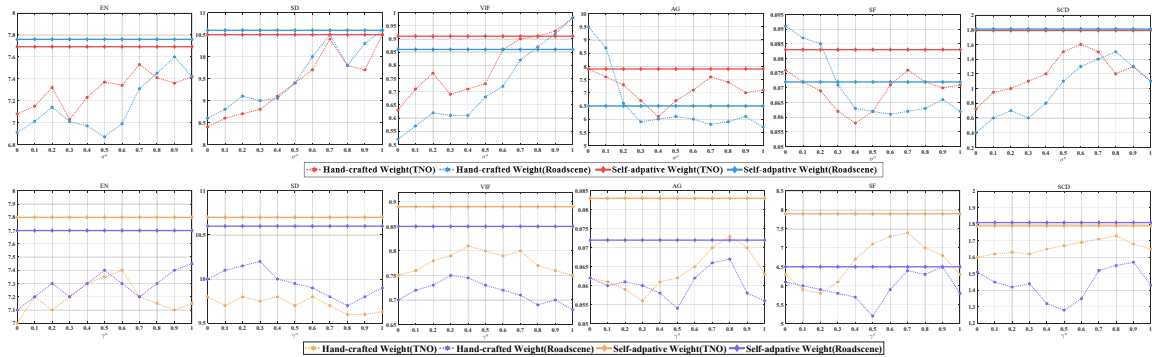


Fig. 12: Quantitative comparison between hand-crafted parameter and our self-adaptive weight on two datasets in terms of σ, γ , respectively. The top row is tested on TNO dataset while the bottom row is verified on Roadscene dataset. In the diagram, dotted lines represent the metric value using manually crafted weight parameters, tuning from 0 to 1. To make the comparison more obvious, the solid line denotes the quantitative value using self-adaptive weight.

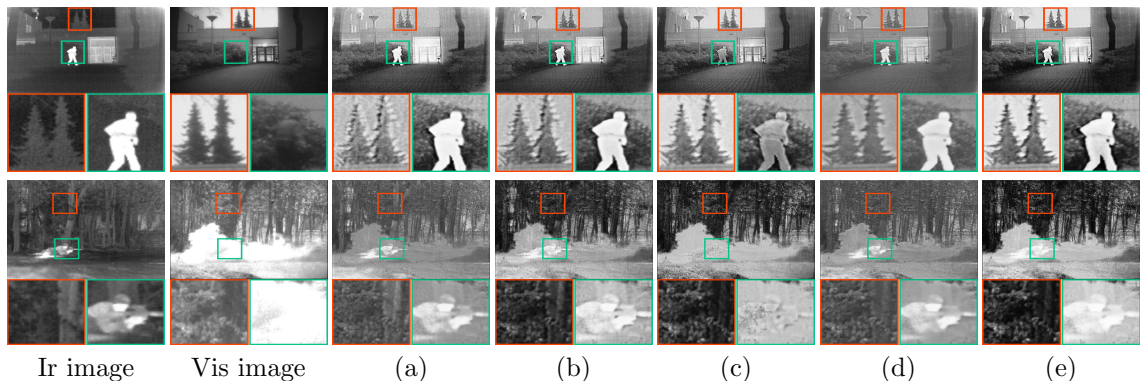


Fig. 13: Visual comparison of different settings of contrastive regularization, where (a) no contrastive regularization, (b) target constrain only, (c) detail constrain only, (d) contrast with random positive and negative samples, and (e) the proposed contrastive regularization. Our method is better in preserving both salient targets and faithful details, especially in the zoomed-in patches. Best viewed on screen.

of six metrics where σ is fixed to a certain value between 0 and 1, while γ is self-adaptive. Likewise, in the second row, γ is hand-crafted, while σ is learned based on source images. We notice that for both SSIM and MSE weights, hand-crafted manner fails to adapt to characteristics in various images, thus reporting lower scores on six evaluation metrics in most cases. On TNO dataset, our strategy achieves around 0.2 points higher than fixed SSIM weights on SCD, which is higher than the best hand-crafted weights. Despite that hand-crafted weights outperform ours on certain points (e.g., fixed weights are slightly better on VIF when σ is set to 0.8), we generate images of higher qualities by employing features from a single image itself, which is robust to source images with diverse characteristics.

Effectiveness of contrastive learning Experiments are further conducted to verify the effectiveness of the proposed contrastive regularization, the visual comparisons can be found in Figure 13, where (a) means results with neither target nor detail constrain, column (b) denotes results with target constrain only and (c) means results with detail constrain only. To better showcase the importance of sample selection in the contrastive regularization, in column (d), we contrast images using samples that are not corresponded to each other (i.e., image patches for contrast are randomly selected from the whole dataset). The full contrastive learning is given in column (e). Obviously, the lack of both infrared and visible contrast brings unwanted noises to the fused results, causing the edge blurry (e.g., in column (a), the tree details in the red boxes are less clearer with noisy pixels). In column (b), we present results with infrared regularization only. Despite enhancement of the salient thermal target, we still notice degradation of image quality on the visible details, making it hard to render vivid textural information. This proves that removing regularization on the visible part could harm textural details in the fusion process. In column (c), we display results with only visible constraints by removing the infrared enhancement. It is obvious that the thermal target (e.g., the standing person indicated by the green box) is abundant in visible details but less bright for the absence of enough guidance of infrared features. Based on results from column (d), we argue that patch sampling is the most significant in contrastive regularization. In absence of correct

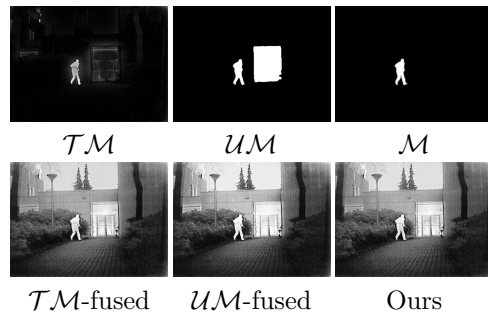


Fig. 14: Different masks and their fusion results.

guidance, the fused image is degraded, with its pixel darker and less clearer, e.g., the person is less brighter and the image appears blurry in general. In conclusion, both target and detail constrains are indispensable to achieve our initial goal, that is, combining both salient thermal targets from the infrared image and vivid background details from the visible image.

Analysis of Different masks We generated the \mathcal{M} in various manners in order to investigate how the \mathcal{M} affects the proposed method. All three kinds of masks are shown in the first line in Figure 14. $\mathcal{T}\mathcal{M}$ is the feature weight map generated by a human detection algorithm [Montabone and Soto \(2010\)](#) guided by the saliency mechanism. In practice, we set a threshold to convert it since it was originally not a 0-1 mask. $\mathcal{U}\mathcal{M}$ comes from an unsupervised saliency detector [Nguyen et al \(2019\)](#), which also marks the door highlighted by room temperature in the infrared image.

We used these three different masks for fusion, and the results are shown in the second line in Figure 14. From the visual perspective, different masks do not affect the visualization features of the proposed method (such as real details and high contrast). The performance of the proposed method is almost independent of how we obtain the masks.

4.4 Computational Complexity Analysis

Beyond qualitative and numerical analysis, model size and running speed are significant in real-world applications as well. Therefore, we verify the memory consumption and computation efficiency of the proposed model. Note that the results shown in this part might be slightly different from the

Table 3: Quantitative comparisons on model complexity and running time.

Method	DenseFuse	FusionGAN	PMGI	DIDFuse	GANMcC	RFN	MFEIF	U2Fusion	SwinFusion	SDNet	SMoA	TarDAL	Ours
TP(M)	0.925	0.074	0.042	0.261	1.864	10.936	0.158	0.659	0.974	0.067	0.223	0.297	9.13
FLOPS(G)	497.96	48.96	745.21	18.71	1002.56	676.09	25.32	366.34	471.04	37.35	61.869	82.37	115.37
Time(s)	0.124	0.251	0.182	0.055	0.246	0.239	0.045	0.123	1.345	0.045	8.071	0.002	0.052

original paper due to different settings of running platform, hyper-parameters, etc. Specifically, FLOPs and training parameters are calculated by setting input size as 64×64 . For running time, we select ten images from TNO with size 64×64 to compute the average time. Table 3 displays quantitative results on model size, FLOPs and running time among several state-of-the-art methods. Our model is faster than all methods except for IFCNN and MFEIF. Although we are slower due to the simplicity of their frameworks, our model still achieves a running time under 0.1s, which is two times faster than DenseFuse and U2Fusion, three times faster than PMGI, and four times faster than FusionGAN, GANMcC and RFN. Moreover, inspite that our CoCoNet is more complicated than FusionGAN, we enjoy faster speed, which demonstrates the strength of the proposed architecture. Specially, MAM module needs large parameters to calculate and integrate the multi-level features for better feature extraction and transmission. Although removing the MAM module can alleviate the computational complexity to some extent, it may lose some vital information during the fusion process, resulting in loss of detail or blurred target on the fused result.

4.5 Limitations

It is pretty challenging to acquire pixel-level aligned infrared and visible image pairs in most real-world scenarios. To discuss the impact of fusing these slight misalignment image pairs, we initially synthesize these slight misaligned source images through performing random affine and elastic translations with different degrees(i.e., tiny, moderate, and extreme) on the TNO, Roadscene datasets, respectively. Then we use the proposed method for merging these misaligned source images. Visual results are shown in Figure ??, note that our method can deal with the slightly misaligned images, which preserves a large part of vital information. However, halos and artifacts

emerge on the fused results when pixel deviation is significant.

4.6 Results and Analysis on MIF

We compare the proposed method with some state-of-the-art approaches, including three traditional methods (i.e., self-adaptive sparse representation based ASR Liu and Wang (2015), convolution sparse representation and morphological principal component analysis based CSMCA Liu et al (2019) and contour wave transform based Curvelet Yang et al (2008)), three CNN-based method (i.e., EMFusion Xu and Ma (2021), SDNet Zhang and Ma (2021) and U2Fusion Xu et al (2020)) and transformer based SwinFusion Ma et al (2022a). As SwinFusion is only able to deal with the MRI-PET image pairs, so that its results only participate in the comparison of MRI-PET fusion task.

4.6.1 MRI-PET fusion task

Qualitative Comparisons The comparisons of visualization on typical MRI-PET images and MRI-SPECT images are shown in Figure 15 and Figure 16. Benefiting from the multi-scale attention mechanism, the proposed method can accurately retain high-value information in different modalities. In addition, the constrative learning using MRI segmentation masks, which successfully solves the problem that MRI image information is covered by intensity information of other modalities, prevents the loss of effective details. The three traditional methods have similar performance. They focus on the preservation of details in MRI, but ignore the restoration of color information in another modality (the frame part of the first two sets of images). SDNet and U2Fusion are difficult to effectively extract and save information, causing serious loss of details and colors, while EMFusion causes serious color distortion (the frame part of the last set of images). SwinFusion retains color information well, but it does not

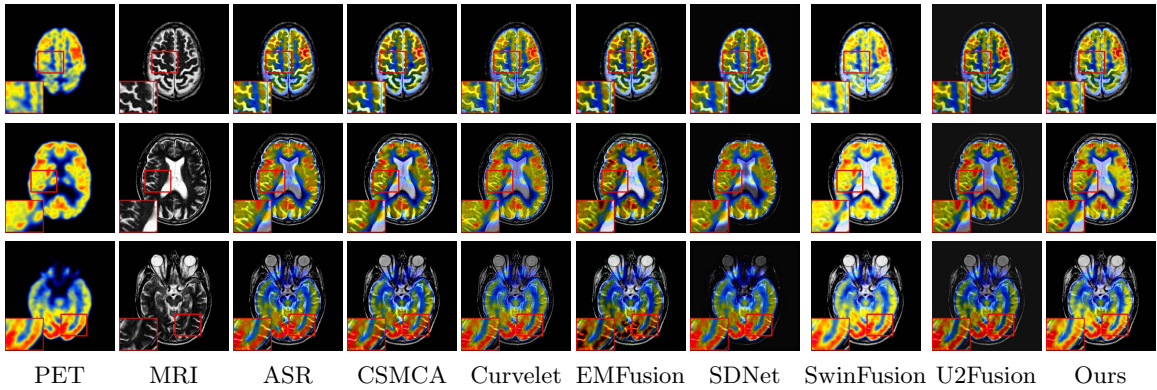


Fig. 15: Visual comparison of different methods on MRI-PET task. Best viewed on screen.

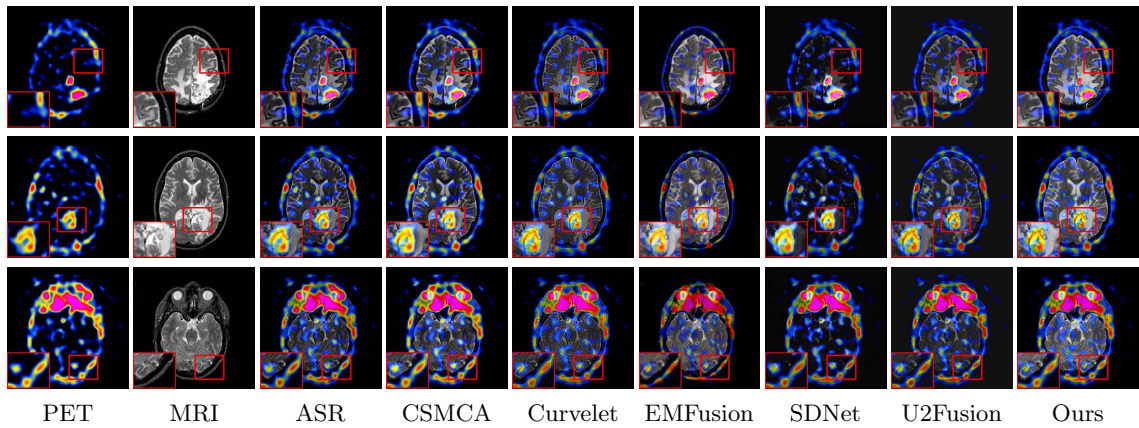


Fig. 16: Visual comparison of different methods on MRI-SPECT task. Best viewed on screen.

solve the problem of MRI details being covered. To sum up, the proposed method achieves the balance between retaining color and detail information, and achieves the optimal visualization effect.

Quantitative Comparisons To give a better view of the performance of CoCoNet on MIF task, we provide the evaluations of all methods on metrics discussed in the above section. The results are shown in the left of Table 4. It is obvious that the proposed method achieves the highest results on

EN, SD, SF, AG and SOTA level on SCD. SwinFusion achieves the highest VIF and SCD results with its characteristic highlighted visualization pictures.

4.6.2 MRI-SPECT fusion task

Qualitative Comparisons Different from pet, intensity information of spect image is more sparse. The MRI segmentation mask constrative learning used can better preserve the details of

Table 4: Quantitative comparisons of MRI-PET and MRI-SPECT image fusion tasks.

Method	MRI-PET						MRI-SPECT					
	EN	SD	VIF	SF	AG	SCD	EN	SD	VIF	SF	AG	SCD
ASR	3.755±0.491	8.658±0.768	0.573±0.056	0.1027±0.0164	6.570±1.306	1.246±0.158	3.922±0.291	8.445±0.336	0.452±0.017	0.0714±0.0033	4.891±0.339	1.060±0.031
CSMCA	3.937±0.524	8.649±0.743	0.645±0.066	0.1071±0.0173	6.919±1.392	1.318±0.170	4.175±0.315	8.431±0.335	0.472±0.018	0.0782±0.0043	5.454±0.427	1.130±0.031
Curvelet	4.206±0.579	8.599±0.777	0.551±0.052	0.0971±0.0151	6.204±1.279	1.152±0.170	4.237±0.280	8.644±0.365	0.502±0.019	0.0740±0.0046	4.885±0.405	1.032±0.028
EMFusion	4.165±0.584	8.516±0.594	0.667±0.056	0.1009±0.0174	6.662±1.412	1.214±0.201	3.928±0.260	8.378±0.485	0.23±0.011	0.0637±0.0029	4.374±0.315	0.585±0.038
SDNet	4.150±0.551	8.089±0.824	0.424±0.046	0.0626±0.0077	3.840±0.588	0.824±0.093	4.084±0.294	6.639±0.237	0.439±0.012	0.0621±0.0054	3.305±0.329	1.004±0.022
U2Fusion	4.088±0.588	7.928±0.693	0.444±0.028	0.0632±0.0076	4.627±0.851	0.616±0.261	3.972±0.272	7.279±0.214	0.256±0.011	0.0543±0.0033	3.800±0.323	0.843±0.036
SwinFusion	4.468±0.664	8.697±0.758	0.722±0.074	0.0772±0.0156	5.902±1.454	1.726±0.078	-	-	-	-	-	-
Ours	4.498±0.359	8.737±0.694	0.645±0.057	0.1081±0.0166	7.049±1.387	1.454±0.240	4.142±0.221	8.871±0.452	0.404±0.022	0.0653±0.0029	4.658±0.317	0.874±0.028

the MRI image with less interference. Other deep learning methods suffer information loss in different degrees and modalities: SDNet and U2Fusion enable to save the details of MRI images, while EMFusion has a serious defect in color information (the frame part of the first set and the last set of images). Traditional methods retain intensity information, but suffer from MRI partial darkening (the frame part of the first two sets of images).

Quantitative Comparisons The evaluations of all methods on metrics are shown in the right side of Table 4. All deep learning methods have disastrous performance on six metrics, but we have achieved SOTA performance upon all depth learning methods. Based on the actual analysis, the reasons are as follows: since the original resolution of spect images is low, the images need to be upsampled before participating in fusion. In this process, many non-uniform pixel noises are introduced, while convolutional neural network can better process them to produce smooth results. In the calculation of indicators, the noise interference produces results unfavorable to the depth learning method, such as EN, SF and AG. Our method better retains the information of the two modalities, so it is superior to other deep learning methods in terms of metrics.

5 CONCLUSION

This paper proposes a novel multi-level attention-guided contrastive learning network for fusing infrared and visible images. We design a multi-level attention in our network to learn rich hierarchical feature representation and ensemble better transmission. We develop twin contrastive constraints to preserve the typical features and remove the redundant features during the fusion process. As a result, the twin contrastive constraints can achieve better visual effects in a soft manner, *i.e.*, salient thermal targets and rich faithful details. Besides, a self-adaptation weight is designed to overcome the limitation of the manually-craft trade-of weight in the loss function. The qualitative and quantitative results demonstrate that the proposed method achieves the SOTA performance with high efficiency. Moreover, ablation experiments valid the effectiveness of our method. Furthermore, we extend our CoCoNet to apply on medical image fusion, and it can also

achieve an superior performance compared with other state-of-the-art approaches.

Acknowledgment

This work is partially supported by the National Key R&D Program of China (2020YFB1313503), the National Natural Science Foundation of China (Nos. 61922019, 61733002, 62027826 and 61772105), LiaoNing Revitalization Talents Program (XLYC1807088), and the Fundamental Research Funds for the Central Universities.

Availability of supporting data

Figures used in this study have been deposited in github

(<https://github.com/runjia0124/CoCoNet>).

References

- Abdi H, Williams LJ (2010) Principal component analysis. Wiley interdisciplinary reviews: computational statistics 2(4):433–459
- Aslantas V, Bendes E (2015) A new image quality metric for image fusion: the sum of the correlations of differences. Aeu-international Journal of electronics and communications 69(12):1890–1896
- Bavirisetti DP (2017) Multi-sensor image fusion based on fourth order partial differential equations. In: 20th International Conference on Information Fusion (Fusion), 2017
- Bhatnagar G, Wu QJ, Liu Z (2013) Directive contrast based multimodal medical image fusion in nsct domain. IEEE TMM 15(5):1014–1024
- Cui G, Feng H, Xu Z, et al (2015) Detail preserved fusion of visible and infrared images using regional saliency extraction and multi-scale image decomposition. Optics Communications 341(341):199–209
- Da Cunha AL, Zhou J, Do MN (2006) The nonsubsampling contourlet transform: theory, design, and applications. IEEE TIP 15(10):3089–3101

- Dosovitskiy A, Beyer L, Kolesnikov A, et al (2020) An image is worth 16x16 words: Transformers for image recognition at scale. arXiv preprint arXiv:201011929
- Duan Z, Lan J, Xu Y, et al (2017) Pedestrian detection via bi-directional multi-scale analysis. In: ACM MM, ACM, pp 1023–1031
- Eskicioglu AM, Fisher PS (1995) Image quality measures and their performance. *IEEE TCOM* 43(12):2959–2965
- Gangapure VN, Nanda S, Chowdhury AS (2017) Superpixel-based causal multisensor video fusion. *IEEE TCSVT* 28(6):1263–1272
- Han Y, Cai Y, Cao Y, et al (2013) A new image fusion performance metric based on visual information fidelity. *Information Fusion* 14(2):127–135
- He K, Fan H, Wu Y, et al (2020) Momentum contrast for unsupervised visual representation learning. In: *IEEE/CVF CVPR*, pp 9729–9738
- Henaff O (2020) Data-efficient image recognition with contrastive predictive coding. In: *ICML*, PMLR, pp 4182–4192
- Huang Z, Wang X, Huang L, et al (2019) Ccnet: Criss-cross attention for semantic segmentation. In: *ICCV*, pp 603–612
- Hyvärinen A, Oja E (2000) Independent component analysis: algorithms and applications. *Neural networks* 13(4-5):411–430
- Jiang Z, Zhang Z, Fan X, et al (2022) Towards all weather and unobstructed multi-spectral image stitching: Algorithm and benchmark. In: *Proceedings of the 30th ACM International Conference on Multimedia*, pp 3783–3791
- Kim M, Han DK, Ko H (2016) Joint patch clustering-based dictionary learning for multi-modal image fusion. *Information Fusion* 27:198–214
- Lewis JJ, O’Callaghan RJ, Nikolov SG, et al (2007) Pixel-and region-based image fusion with complex wavelets. *Information fusion* 8(2):119–130
- Li H, Wu XJ (2018) Densefuse: A fusion approach to infrared and visible images. *IEEE TIP* 28(5):2614–2623
- Li H, Wu XJ, Kittler J (2018a) Infrared and visible image fusion using a deep learning framework. In: *2018 24th International Conference on Pattern Recognition (ICPR)*, IEEE, pp 2705–2710
- Li H, Wu XJ, Kittler J (2021) Rfn-nest: An end-to-end residual fusion network for infrared and visible images. *Information Fusion* 73:72–86
- Li S, Kang X, Hu J (2013) Image fusion with guided filtering. *IEEE TIP* 22(7):2864–2875
- Li W, Du J, Zhao Z, et al (2018b) Fusion of medical sensors using adaptive cloud model in local laplacian pyramid domain. *IEEE TBE* 66(4):1172–1183
- Li X, Zhong Z, Wu J, et al (2019) Expectation-maximization attention networks for semantic segmentation. In: *ICCV*, pp 9167–9176
- Li Y, Chi Z (2005) Mr brain image segmentation based on self-organizing map network. *International Journal of Information Technology* 11(8):45–53
- Liu J, Fan X, Jiang J, et al (2021a) Learning a deep multi-scale feature ensemble and an edge-attention guidance for image fusion. *IEEE TCSVT*
- Liu J, Shang J, Liu R, et al (2021b) Halder: Hierarchical attention-guided learning with detail-refinement for multi-exposure image fusion. In: *ICME*, IEEE, pp 1–6
- Liu J, Wu Y, Huang Z, et al (2021c) Smoa: Searching a modality-oriented architecture for infrared and visible image fusion. *IEEE Signal Processing Letters* 28:1818–1822
- Liu J, Fan X, Huang Z, et al (2022a) Target-aware dual adversarial learning and a multi-scenario multi-modality benchmark to fuse infrared and visible for object detection. In: *Proceedings of the IEEE/CVF Conference on Computer Vision and Pattern Recognition*, pp 5802–5811

- Liu R, Liu J, Jiang Z, et al (2021) A bilevel integrated model with data-driven layer ensemble for multi-modality image fusion. *IEEE TIP* 30:1261–1274
- Liu R, Jiang Z, Yang S, et al (2022b) Twin adversarial contrastive learning for underwater image enhancement and beyond. *IEEE Transactions on Image Processing* 31:4922–4936
- Liu R, Ma L, Ma T, et al (2022c) Learning with nested scene modeling and cooperative architecture search for low-light vision. *IEEE Transactions on Pattern Analysis and Machine Intelligence*
- Liu Y, Wang Z (2015) Simultaneous image fusion and denoising with adaptive sparse representation. *IET Image Processing* 9(5):347–357
- Liu Y, Liu S, Wang Z (2015) A general framework for image fusion based on multi-scale transform and sparse representation. *Information fusion* 24:147–164
- Liu Y, Chen X, Ward RK, et al (2019) Medical image fusion via convolutional sparsity based morphological component analysis. *IEEE Signal Processing Letters* 26(3):485–489
- Liu Z, Lin Y, Cao Y, et al (2021) Swin transformer: Hierarchical vision transformer using shifted windows. In: *Proceedings of the IEEE/CVF International Conference on Computer Vision*, pp 10,012–10,022
- Lu X, Zhang B, Zhao Y, et al (2014) The infrared and visible image fusion algorithm based on target separation and sparse representation. *Infrared Physics & Technology* 67:397–407
- Lv F, Li Y, Lu F (2019) Attention guided low-light image enhancement with a large scale low-light simulation dataset. *arXiv preprint arXiv:190800682*
- Ma J, Chen C, Li C, et al (2016) Infrared and visible image fusion via gradient transfer and total variation minimization. *Information Fusion* 31:100–109
- Ma J, Zhou Z, Wang B, et al (2017) Infrared and visible image fusion based on visual saliency map and weighted least square optimization. *Infrared Physics & Technology* 82:8–17
- Ma J, Ma Y, Li C (2019a) Infrared and visible image fusion methods and applications: A survey. *Information Fusion* 45:153–178
- Ma J, Yu W, Liang P, et al (2019b) FusionGAN: A generative adversarial network for infrared and visible image fusion. *Information Fusion* 48:11–26
- Ma J, Xu H, Jiang J, et al (2020a) DdGAN: A dual-discriminator conditional generative adversarial network for multi-resolution image fusion. *IEEE TIP* 29:4980–4995
- Ma J, Zhang H, Shao Z, et al (2020b) GanMCC: A generative adversarial network with multi-classification constraints for infrared and visible image fusion. *IEEE TIM* 70:1–14
- Ma J, Tang L, Fan F, et al (2022a) SwinFusion: Cross-domain long-range learning for general image fusion via swin transformer. *IEEE/CAA Journal of Automatica Sinica* 9(7):1200–1217
- Ma L, Ma T, Liu R, et al (2022b) Toward fast, flexible, and robust low-light image enhancement. In: *Proceedings of the IEEE/CVF Conference on Computer Vision and Pattern Recognition*, pp 5637–5646
- Meng F, Song M, Guo B, et al (2017) Image fusion based on object region detection and non-subsampled contourlet transform. *Computers & Electrical Engineering* 62:375–383
- Montabone S, Soto A (2010) Human detection using a mobile platform and novel features derived from a visual saliency mechanism. *Image and Vision Computing* 28(3):391–402
- Nguyen T, Dax M, Mummadi CK, et al (2019) DeepUSPS: Deep robust unsupervised saliency prediction via self-supervision. *Advances in Neural Information Processing Systems* 32
- Parikh AP, Täckström O, Das D, et al (2016) A decomposable attention model for

- natural language inference. arXiv preprint arXiv:160601933
- Petrovic VS, Xydeas CS (2004) Gradient-based multiresolution image fusion. *IEEE TIP* 13(2):228–237
- Pu M, Huang Y, Guan Q, et al (2018) Graphnet: learning image pseudo annotations for weakly-supervised semantic segmentation. In: *ACM MM*, ACM, pp 483–491
- Roberts WJ, Van JAA, Ahmed F (2008) Assessment of image fusion procedures using entropy, image quality, and multispectral classification. *Journal of Applied Remote Sensing* 2(1):1–28
- Simonyan K, Zisserman A (2014) Very deep convolutional networks for large-scale image recognition. arXiv preprint arXiv:14091556
- Tu TM, Huang PS, Hung CL, et al (2004) A fast intensity-hue-saturation fusion technique with spectral adjustment for ikonos imagery. *IEEE GRSL* 1(4):309–312
- Vaswani A, Shazeer N, Parmar N, et al (2017a) Attention is all you need. *Advances in neural information processing systems* 30
- Vaswani A, Shazeer N, Parmar N, et al (2017b) Attention is all you need. In: *Advances in neural information processing systems*, pp 5998–6008
- VS V, Valanarasu JMJ, Oza P, et al (2021) Image fusion transformer. arXiv preprint arXiv:210709011
- Wang Z, Bovik AC, Sheikh HR, et al (2004) Image quality assessment: from error visibility to structural similarity. *IEEE TIP* 13(4):600–612
- Wong MH, Giraldo JP, Kwak SY, et al (2017) Nitroaromatic detection and infrared communication from wild-type plants using plant nanobionics. *Nature materials* 16(2):264–271
- Wu H, Qu Y, Lin S, et al (2021) Contrastive learning for compact single image dehazing. In: *IEEE/CVF CVPR*, pp 10,551–10,560
- Xie E, Ding J, Wang W, et al (2021) Detco: Unsupervised contrastive learning for object detection. In: *ICCV*, pp 8392–8401
- Xu H, Ma J (2021) Emfusion: An unsupervised enhanced medical image fusion network. *Information Fusion* 76:177–186
- Xu H, Liang P, Yu W, et al (2019) Learning a generative model for fusing infrared and visible images via conditional generative adversarial network with dual discriminators. In: *IJCAI-19*, pp 3954–3960
- Xu H, Ma J, Jiang J, et al (2020) U2fusion: A unified unsupervised image fusion network. *IEEE TPAMI*
- Yan X, Qin H, Li J, et al (2015) Infrared and visible image fusion with spectral graph wavelet transform. *JOSA A* 32(9):1643–1652
- Yang L, Guo BL, Ni W (2008) Multimodality medical image fusion based on multiscale geometric analysis of contourlet transform. *Neurocomputing* 72(1):203–211
- Yin M, Duan P, Liu W, et al (2017) A novel infrared and visible image fusion algorithm based on shift-invariant dual-tree complex shearlet transform and sparse representation. *Neurocomputing* 226:182–191
- Zhang H, Ma J (2021) Sdnet: A versatile squeeze-and-decomposition network for real-time image fusion. *International Journal of Computer Vision* 129(10):2761–2785
- Zhang H, Xu H, Xiao Y, et al (2020a) Rethinking the image fusion: A fast unified image fusion network based on proportional maintenance of gradient and intensity. In: *AAAI*, pp 12,797–12,804
- Zhang J, Lu S, Zhan F, et al (2021a) Blind image super-resolution via contrastive representation learning. arXiv preprint arXiv:210700708
- Zhang Q, Fu Y, Li H, et al (2013) Dictionary learning method for joint sparse representation-based image fusion. *Optical Engineering* 52(5):057,006–1–057,006–11

- Zhang Q, Liu Y, Blum RS, et al (2018) Sparse representation based multi-sensor image fusion for multi-focus and multi-modality images: A review. *Information Fusion* 40:57–75
- Zhang Y, Li K, Li K, et al (2019) Residual non-local attention networks for image restoration. arXiv preprint arXiv:190310082
- Zhang Y, Liu Y, Sun P, et al (2020b) Ifcnn: A general image fusion framework based on convolutional neural network. *Information Fusion* 54:99–118. <https://doi.org/https://doi.org/10.1016/j.inffus.2019.07.011>, URL <https://www.sciencedirect.com/science/article/pii/S1566253518305505>
- Zhang Z, Lin Z, Xu J, et al (2021b) Bilateral attention network for rgb-d salient object detection. *IEEE TIP* 30:1949–1961
- Zhao W, Lu H, Wang D (2018) Multisensor image fusion and enhancement in spectral total variation domain. *IEEE TMM* 20(4):866–879
- Zhao Z, Xu S, Zhang C, et al (2020a) Did-fuse: Deep image decomposition for infrared and visible image fusion. arXiv preprint arXiv:200309210
- Zhao Z, Xu S, Zhang C, et al (2020b) Bayesian fusion for infrared and visible images. *Signal Processing* 177:107,734